



Article

Numerical Study on the Surface Plasmon Resonance Tunability of Spherical and Non-Spherical Core-Shell Dimer Nanostructures

Joshua Fernandes and Sangmo Kang *

Department of Mechanical Engineering, Dong-A University, Busan 49315, Korea; joshuafernandes95@gmail.com

* Correspondence: kangsm@dau.ac.kr

Abstract: The near-field enhancement and localized surface plasmon resonance (LSPR) on the core-shell noble metal nanostructure surfaces are widely studied for various biomedical applications. However, the study of the optical properties of new plasmonic non-spherical nanostructures is less explored. This numerical study quantifies the optical properties of spherical and non-spherical (prolate and oblate) dimer nanostructures by introducing finite element modelling in COMSOL Multiphysics. The surface plasmon resonance peaks of gold nanostructures should be understood and controlled for use in biological applications such as photothermal therapy and drug delivery. In this study, we find that non-spherical prolate and oblate gold dimers give excellent tunability in a wide range of biological windows. The electromagnetic field enhancement and surface plasmon resonance peak can be tuned by varying the aspect ratio of non-spherical nanostructures, the refractive index of the surrounding medium, shell thickness, and the distance of separation between nanostructures. The absorption spectra exhibit considerably greater dependency on the aspect ratio and refractive index than the shell thickness and separation distance. These results may be essential for applying the spherical and non-spherical nanostructures to various absorption-based applications.

Keywords: electromagnetic field enhancement; localized surface plasmon resonance; plasmonic nanostructures; aspect ratio; refractive index; shell thickness; distance of separation



Citation: Fernandes, J.; Kang, S. Numerical Study on the Surface Plasmon Resonance Tunability of Spherical and Non-Spherical Core-Shell Dimer Nanostructures. *Nanomaterials* **2021**, *11*, 1728. <https://doi.org/10.3390/nano11071728>

Academic Editor: Pablo del Pino

Received: 27 May 2021
Accepted: 28 June 2021
Published: 30 June 2021

Publisher's Note: MDPI stays neutral with regard to jurisdictional claims in published maps and institutional affiliations.



Copyright: © 2021 by the authors. Licensee MDPI, Basel, Switzerland. This article is an open access article distributed under the terms and conditions of the Creative Commons Attribution (CC BY) license (<https://creativecommons.org/licenses/by/4.0/>).

1. Introduction

Plasmonic core-shell nanoparticles are one of the most powerful optical and thermal contrast agents in the field of biomedicine [1–4] with a lot of attention drawn towards cancer treatment [5–7]. The strong interaction of these metal nanoparticles (MNPs), with the incident electromagnetic field allows them to exhibit unique optical properties [8]. The collective free electron oscillation in the nanoparticles gives rise to the localized surface plasmon resonance (LSPR) effect, which can result in the enhancement of absorption and scattering of the incident electromagnetic waves [9–13]. Gold nanoparticles have gained a lot of attention because of their strong optical absorption capacity and high resonance wavelength tunability [14]. The maximization of near-field enhancement in the gold nanoparticles depends strongly on the geometrical aspects, dielectric properties, and compositional factors [15–19]. Small differences in the geometrical features will lead to shifts in the optical properties of these nanoparticles, and the resulting resonance wavelengths can span from visible to near-infrared (NIR) regions. In order to obtain deeper penetration of light into the human tissues, ideal nanomaterials that can strongly absorb energy in the optical window have to be developed.

In recent years, the LSPR characteristics of nanospheres and nanorods, among several other nanostructures, have been studied [20–22]. Researchers have successfully used the Mie theory and discrete dipole approximation (DDA) methods to investigate the optical properties of different gold nanostructures [7]. Extensive Mie theory calculations reveal that the plasmon resonance wavelength maximum shifts almost exponentially as we move

from a solid gold nanosphere (AuNP) to a gold nanoshell (AuNS) with decreasing shell thickness [23]. Among all gold nanoparticles, the ultra-thin hollow gold nanoshells (AuNSs) produced by the synthesis of cobalt (Co) nanoparticles as sacrificial templates induce a unique tunable absorption band in the near-infrared tissue window of 650–950 nm (NIR-I window), where tissues are maximally transparent [24–27]. AuNSs demonstrating plasmon resonance in this tissue window, exhibit strong absorption and scattering characteristics depending on their morphology and can be useful bioimaging and photothermal ablation agents [28,29]. The gold shell filled with the aqueous embedding medium should be large enough to allow prolonged blood circulation time for biomedical applications [30–32].

Upon coupling of two identical core-shell nanoparticles to form a dimer, plasmonic modes with high field enhancement in the gap of nanoshells occur due to the dipolar mode coupling of the individual particles [33]. Due to the occurrence of an extremely intense electric field confinement in the nanogap, the dimer structures are drawing attention in the optical techniques. Experimental and theoretical advances are currently being made in the field of plasmonics, specifically the near-field enhancement in core-shell dimer nanostructures. The low energy absorption and minimal scattering in the NIR-II window (1000–1700 nm) provide better tissue transmission rate and lower photon scattering for the incident light, which is highly suitable for biomedical applications and photoacoustic imaging [34–36]. Compared to the NIR-I window, the larger penetration depth and higher maximum permissible exposure (MPE) to the laser are clear advantages of working in the NIR-II window. However, very few studies have been performed in the NIR-II window because of the lack of photosensitive materials of morphology needed to attain high photothermal efficiency in this tissue window [37,38]. It is noteworthy that no numerical investigation of the plasmonic properties of non-spherical dimer nanostructures is explored. This motivates us to investigate models of prolate and oblate-shaped non-spherical dimer nanostructures to determine their LSPR peaks and absorption cross-sections. Thus, the present study aims at scrutinizing aspects affecting the resonance frequency and enhancement factor for the gold-based nanostructures.

In this study, we numerically study the optical properties of core-shell nanoparticle dimers of spherical and spheroidal (non-spherical) shapes. The finite element modelling study is performed using a commercial software COMSOL Multiphysics to describe the localized surface plasmon resonance behaviour in the region of separation of the dimer nanostructures. This study compares the optical properties obtained using the non-spherical prolate and oblate dimer nanostructures with those of the spherical dimer nanoshells. The effects of varying the aspect ratio, refractive index of the surrounding medium, shell thickness while maintaining a constant outer radius, and distance of separation between nanostructures are studied. The results clearly show that a wide range of tunability of the LSPR peaks in the NIR windows can be obtained for the non-spherical prolate and oblate nanostructures when compared to the spherical nanoshell dimer. The remainder of this study is organized by first including the theoretical equations and numerical method. Secondly, the validation of the numerical method and the effect of the aspect ratio on the LSPR is investigated for the gold nanostructures. Thirdly, the dependence of LSPR on the refractive index of the surrounding medium is studied for the spherical and non-spherical gold nanostructures by using different refractive indices for the surrounding medium. Finally, we solve the absorption cross-section and electromagnetic field enhancement factor by varying the shell thickness and distance of separation between core-shell nanostructures.

2. Numerical Method

The numerical study of the optical properties of plasmonic nanostructures using the finite element method (FEM)-based solver is one of the best alternative methods for the complex analytical solution to problems involving multiple nanostructures. The schematic diagrams of core-shell plasmonic dimer nanostructures with a gold shell and a core made of an aqueous medium are depicted in Figure 1. We perform a 3D modelling and simulation study based on FEM using a versatile commercial software package COMSOL Multiphysics.

The optical properties of core-shell structured nanoparticles are calculated using the wave optics module in COMSOL Multiphysics. The spherical and non-spherical dimers are illuminated by an incident plane wave propagating along the z -axis and the electric field polarization along the x -axis with the background electric field $E_b = E_0 \exp(-jk_0z)$. Here, E_0 is the incident electric field, which is set to unity in this numerical study, and k_0 is the free space wave number. Assuming that the electric field is time harmonic, the electric field distribution \mathbf{E} is computed using the Helmholtz equation and represented as follows [39]:

$$\nabla \times (\mu_r^{-1} \nabla \times \mathbf{E}) - k_0^2 \left(\epsilon_r - j \frac{\sigma}{\omega \epsilon_0} \right) \mathbf{E} = 0, \quad (1)$$

where μ_r is the relative permeability, which is taken as unity, ω is the frequency of the incident light, ϵ_0 is the permittivity of free space, σ is the conductivity, and ϵ_r is the relative permittivity. The relative permittivity, $\epsilon_r = \epsilon/\epsilon_0$, is a frequency-dependent complex dielectric quantity for the gold shell, henceforth symbolized as ϵ_{Au} in this study. Moreover, as the thickness of the thin metal shell becomes comparable to the mean free path of conduction electrons (~ 42 nm), the size effect of bound electrons and interband transition must also be taken into consideration when calculating the dielectric constant of metal shell [40]. Thus, the complex dielectric function of gold ϵ_{Au} is introduced by using the Drude-Lorentz model as follows [41]:

$$\epsilon_{\text{Au}} = \epsilon_{\text{Au-exp}} + \frac{\omega_p^2}{\omega(\omega + i\gamma_{\text{bd}})} - \frac{\omega_p^2}{\omega(\omega + i(\gamma_{\text{bd}} + \gamma_{\text{sd}}))}, \quad (2)$$

where $\epsilon_{\text{Au-exp}}$ is the bulk dielectric function for gold [42], and ω_p , γ_{bd} , and γ_{sd} are the plasma frequency, bulk damping, and damping due to surface scattering, respectively [41]. The damping due to surface scattering is added to the bulk damping in Equation (2) to obtain the corrected dielectric function for the shell material and is given by [43]:

$$\gamma_{\text{sd}} = \frac{Av_f}{l_{\text{eff}}}. \quad (3)$$

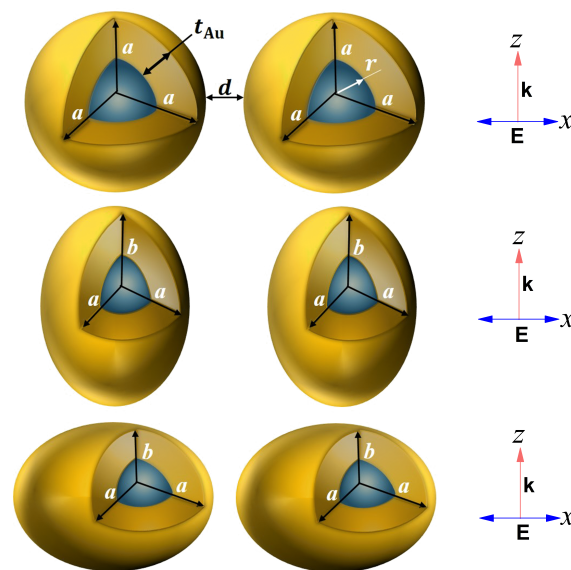


Figure 1. Schematic diagrams of the spherical and non-spherical core-shell nanostructures (top row: spherical, middle: prolate, bottom: oblate). a and b are the semi-principal axes of the nanostructures, d is the distance of separation between the outer surfaces of the nanostructures, t_{Au} is the Au shell thickness, and r is the core radius for the spherical Au nanoshell (AuNS). \mathbf{k} is the incident plane wave along the z -axis, and \mathbf{E} is the electric field polarization along the x -axis.

Here, the phenomenological dimensionless fitting parameter A ranges from 0 to 1 describing the nature of surface scattering and is taken as unity in all simulations [44]. v_f is the Fermi velocity of carrier electrons in the gold shell ($1.40 \times 10^6 \text{ ms}^{-1}$), and the effective mean free path of the electrons l_{eff} in the shell is taken to be equal to the thickness of the gold shell t_{Au} . Perfectly matched layers (PMLs) together with a scattering type boundary condition are used to absorb the waves outgoing from the finite-sized computational field that emulates an infinite domain.

The relative absorption and scattering ability of the core-shell nanostructures can be obtained by defining the absorption and scattering cross-sections, σ_{abs} and σ_{sca} , as follows [45,46]:

$$\sigma_{\text{abs}} = \frac{1}{I_0} \iiint Q_r dV, \quad (4)$$

$$\sigma_{\text{sca}} = \frac{1}{I_0} \iint (\mathbf{n} \cdot \mathbf{S}_{\text{sca}}) dS, \quad (5)$$

where Q_r is the power loss density in the nanostructures, \mathbf{n} denotes the normal vector pointing outward from the surface of the nanostructures, \mathbf{S}_{sca} stands for the Poynting vector (Wm^{-2}), V and S are the volume and surface area of the nanostructures, respectively, and $I_0 = \epsilon_0 n E_0^2 / 2$ represents the intensity of the incident wave of amplitude E_0 in the surrounding medium of refractive index n . The enhancement of the incident electromagnetic field in the AuNSs by several orders of magnitude, leads to numerous absorption and scattering-based applications, such as surface enhanced Raman scattering [47], tip-enhanced Raman spectroscopy [48], or drug delivery. $I_0 = \epsilon_0 n E_0^2 / 2$ indicates that the local field intensity of the incident wave at a specific point is proportional to the square of the electric field amplitude. The electromagnetic local field enhancement factor (LFEF) at a particular position (r_0) in the vicinity of the nanostructures can be given as the ratio of the electric field amplitude at that position ($E(r_0)^2$) to the electric field amplitude of the incident wave (E_0^2). Taking into account the dependency of LFEF on the frequency (ω_0) of the incident wave, the LFEF as a function of the position and frequency can be represented as $\text{LFEF}(r_0, \omega_0)$. In addition, the incoming incident wave at ω_0 , while emitting a scattered photon, causes the strong mutual excitation between the dipoles of molecules and nanostructures at the Raman scattered frequency (ω_R). This gives rise to the local field enhancement at the Raman frequency, and the enhancement factor can be represented as $\text{LFEF}(r_0, \omega_R)$. The total electromagnetic enhancement factor (EF) can be expressed by the fourth power relation and can be given as [49]:

$$\text{EF} = \text{LFEF}(r_0, \omega_0) \text{LFEF}(r_0, \omega_R) = \frac{|E(r_0, \omega_0)|^2}{|E_0(r_0, \omega_0)|^2} \frac{|E(r_0, \omega_R)|^2}{|E_0(r_0, \omega_R)|^2} \approx \frac{|E(r_0, \omega_R)|^4}{|E_0(r_0, \omega_0)|^4}. \quad (6)$$

Here, the first enhancement is due to the coupling of plasmons and incident photons, and the second enhancement is due to the coupling of plasmons and emitted photons [50,51]. The fourth power relation is obtained by taking into consideration an assumption that the Raman scattered frequency is close enough to the frequency of incident wave ($\omega_R \approx \omega_0$).

3. Results and Discussion

The optical properties of core-shell nanostructures depend strongly on the size and shape of the nanostructures and their surrounding environment. The spherical, prolate and oblate-shaped nanostructures are numerically simulated to analyse the interaction of the incident light with the dimer configurations. The effects of various core-shell dimer parameters on the optical properties and tuning sensitivity are studied for all three types of nanostructures. The total radius of the spherical AuNS and the effective radius of the non-spherical prolate and oblate nanostructures are kept similar throughout this study for comparisons of the numerically simulated optical properties. The spherical core-shell

nanoparticle dimer is composed of an inner core with radius r (nm) and a gold shell with the thickness t_{Au} (nm), having an interparticle distance d (nm). The effective radius of the non-spherical prolate and oblate nanostructures is given by the term $r_{\text{eff}} = \sqrt[3]{abc}$, where a , b , and c are the semi-principal axes of the non-spherical nanostructures. In all simulations, the values of a and c are kept identical ($a = c$), and the aspect ratios for the non-spherical prolate and oblate structures are defined as $\eta = b/a$ and $\eta = a/b$, respectively. Note that, $\eta = 1$ represents the case of spherical nanostructures.

3.1. Numerical Validation

In order to validate our numerical approach that consists mainly of FEM using COMSOL Multiphysics package (Version 5.6, COMSOL, Inc. Burlington, MA), we simulate two cases, AuNP and AuNS, whose absorption characteristics are available in the literature [52]. The absorption cross-sections for a AuNP and a AuNS for the wavelength range of 450–800 nm are depicted in Figure 2a,b, respectively. The present numerical approach is validated by comparing the numerically obtained absorption cross-sections with those of Oldenburg et al. [52] using the Mie theory. Our numerical results for both nanostructures are in excellent agreement with the theoretical results derived using the Mie theory, indicating that our numerical investigation is accurate enough for the purpose of this study.

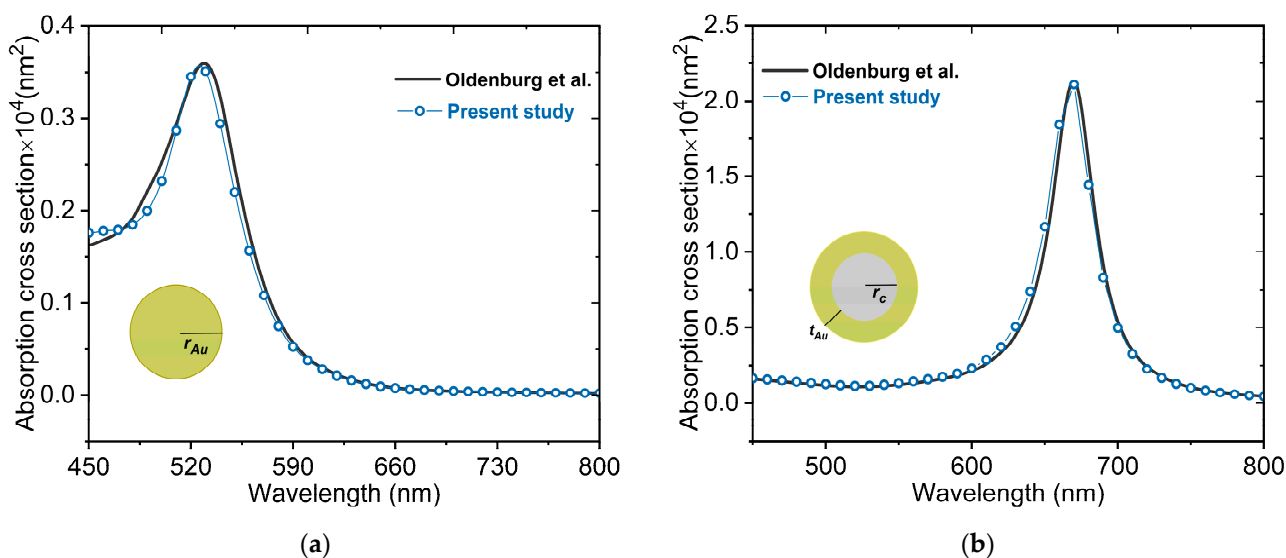


Figure 2. Validation of the present numerical model: Absorption spectra for the (a) solid gold nanoparticle (AuNP) ($r_{\text{Au}} = 20$ nm) and (b) silica-gold core-shell nanoshell ($r_c = 20$ nm, $t_{\text{Au}} = 3$ nm) as a function of the incident wavelength, compared to the Mie theory [52]. The nanostructures are surrounded by water with a refractive index of 1.33.

3.2. Mesh Independence Test

A mesh independence test with identical physical and optical parameters but with a variable number of mesh elements is performed to establish the accuracy of our numerical study. A tetrahedral meshing scheme is adopted for the modelling of the spherical and non-spherical nanostructures. The PMLs with a spherical type swept mesh having 5 elements across the diameter are used to reduce the reflections in the interior, which then provides a better convergence of the solver and maximizes the absorption of the propagating wave. For an increase in the total number of elements from $N \approx 207622$ to ≈ 324052 , the maximum change in the LSPR peak is 0.01%, as shown in Figure 3. By taking into consideration the computational cost and independence of mesh, the mesh comparable qualitatively to $N \approx 207622$ is employed for all numerical simulations performed in this study.

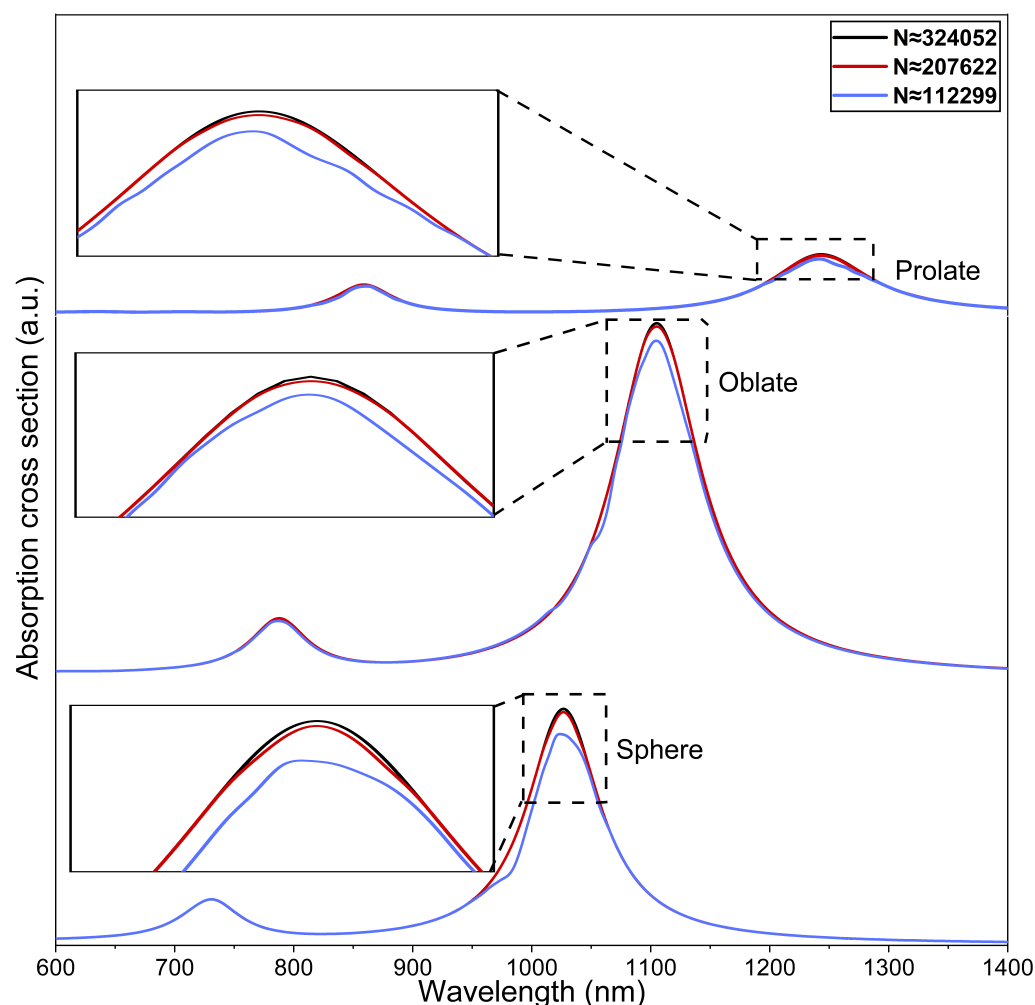


Figure 3. Mesh independence test: Absorption cross sections for the spherical ($r = 20$ nm, $t_{\text{Au}} = 3$ nm) and non-spherical ($r_{\text{eff}} = 23$ nm, $\eta = 3$) core-shell nanostructures. The nanostructures are surrounded by water with a refractive index of 1.33. Here, N is the total number of mesh elements used in the present study.

3.3. Aspect Ratio of Prolate and Oblate Nanostructures

The spectral characteristics of the spheroidal core-shell nanostructures with prolate and oblate shapes having an effective radius of $r_{\text{eff}} = 23$ nm and a shell thickness of $t_{\text{Au}} = 3$ nm for different aspect ratios are shown in Figure 4. The core is considered to be made of an aqueous medium with a refractive index of 1.33. The longitudinal polarization of light for strongly interacting dimers is considered for both nanostructures, as shown in Figure 4a,b. As can be seen in Figure 4a, the maximum absorption cross-section for the prolate spheroid nanostructure is 1.71×10^4 nm² at an aspect ratio $\eta = 2$. The corresponding peak resonance wavelength for this absorption peak is 1095 nm, which occurs in the lower wavelength range of the NIR-II window. However, as η increases from 2 to 6, a significant increase in the amount of red-shift is observed in the absorption spectrum. The wavelength corresponding to the peak resonance at $\eta = 6$ is located near 1765 nm, which is away and beyond the NIR-II window. This implies that for the prolate structure, the LSPR peak can be rigorously red-shifted, specifically providing an extensive range of tunability in the NIR-II window by changing the aspect ratio. For the sake of comparison between the spherical and non-spherical Au nanostructures, the absorption cross-section for the spherical AuNS dimer ($\eta = 1$) is also shown in Figure 4a,b (black dashed curves). It is noteworthy that the intensity of the LSPR peak for the spherical AuNS dimer is higher than that for the prolate dimer nanostructure. However, it is clear from Figure 4a that the

position of the LSPR peak for the prolate dimer exhibits excellent tunability in the NIR windows. In addition, the occurrence of plasmon modes in the shorter wavelength range is primarily due to the dipolar plasmon resonances and close proximity of the two prolate nanostructures.

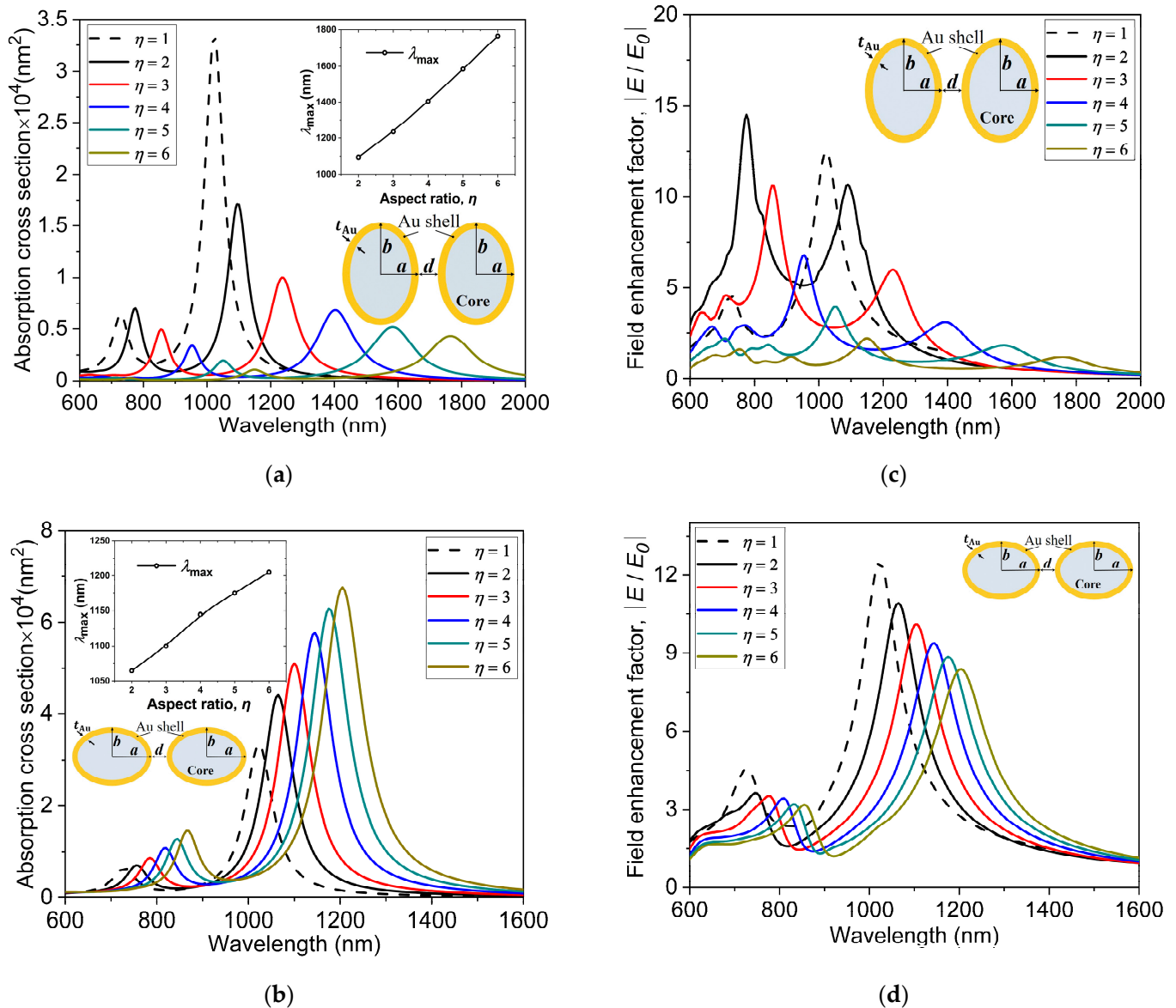


Figure 4. Absorption cross-sections at different aspect ratios for the (a) prolate and (b) oblate core-shell nanostructures ($r_{\text{eff}} = 23$ nm, $n = 1.33$). The insets in panels (a) and (b) show the dependence of the LSPR peak position (λ_{max}) on the aspect ratio. The electric field enhancement $|E/E_0|$ at different aspect ratios for the (c) prolate and (d) oblate nanostructures. The absorption cross-sections and electric field enhancement for the spherical core-shell dimer nanostructures ($\eta = 1$) are also shown for comparison (black dashed curves).

Figure 4b shows the absorption cross-sections at different aspect ratios for the oblate spheroid. The amount of red-shift in the LSPR position in the longer wavelength range is much smaller than that for the prolate dimer nanostructure. However, as the aspect ratio increases, the peak of absorption cross-section is found to remarkably increase, which is opposite to the absorption cross-section response for the prolate dimer nanostructures. The LSPR peak for the aspect ratio $\eta = 6$ is 1.5 times the value obtained for $\eta = 2$ (the corresponding wavelengths are 1205 nm for $\eta = 6$ and 1065 nm for $\eta = 2$). Although the range of the absorption spectrum can be tuned to a certain extent in the NIR-II window

for the oblate dimer nanostructures, it is not as wide as the range of the prolate dimer nanostructures for the same aspect ratios. The insets in the two panels (a) and (b) display the variations of the wavelength corresponding to the LSPR peak with the aspect ratio for the spheroidal nanostructures. The electric field enhancements, $|E/E_0|$, at different aspect ratios are presented in Figure 4c,d for the prolate and oblate nanostructures, respectively. A clear red-shift in $|E/E_0|$ on the surface of prolate and oblate nanostructures together with a decrease in magnitudes can be seen in the panels. The peaks of near-field enhancement are distributed across a wide wavelength range, with the peak values ranging extensively from 1.2 to 14.5 in the two biological windows (NIR-I and NIR-II).

3.4. Refractive Index of the Surrounding Medium

The absorption spectrum of a gold-based nanostructure depends on numerous parameters such as the morphology of nanostructures, incident electromagnetic field, and refractive index (n) of the surrounding medium [53]. The refractive index of the surrounding medium is one of the main factors on which the sensitivity of the LSPR depends. In this subsection, we investigate the effect of varying the refractive index, n , on the absorption spectrum to clearly understand the surrounding medium-dependent optical characteristics of gold nanostructures of spherical and non-spherical shapes. The two spherical AuNSs ($r = 20$ nm, $t_{\text{Au}} = 3$ nm) are separated by a distance of $d = 1$ nm (the distances between the outer surfaces of the nanostructures) in all simulations. In order to compare the absorption spectrum of the spherical AuNS dimer to the non-spherical prolate and oblate dimer nanostructures, the total effective radii (r_{eff}) of the non-spherical nanostructures are kept the same as the total radius of the spherical AuNS, together with an aspect ratio of $\eta = 3$.

To understand the sensitivity of absorption spectra of the spherical and non-spherical nanostructures to the change in the refractive index of the surrounding medium, we perform a set of numerical simulations by placing the nanostructures in solvents of different refractive indices. As shown in Figure 5a, as the refractive index increases from $n = 1.33$ (water) to 1.49 (toluene), a clear red-shift in the LSPR peak for the spherical AuNS dimer is observed. The lower energy plasmon modes occurring in the longer wavelength region (NIR-II window) and the higher energy secondary modes occurring in the shorter wavelength region (NIR-I window) indicate that they can be easily tuned in the two biological windows by varying the refractive index of the solvent. Similar kinds of absorption spectra can be observed for the non-spherical prolate and oblate nanostructures, as depicted in Figure 5b,c respectively. Besides, the amount of red-shift is significantly greater for the non-spherical nanostructures as opposed to the spherical nanostructure. The wavelengths corresponding to the LSPR positions at $n = 1.49$ for the spherical, oblate, and prolate nanostructures are 1100 nm, 1220 nm, and 1380 nm, respectively. The plasmon resonance peaks and their positions for these spherical and non-spherical gold nanostructures exhibit great dependency on the real part of the dielectric constant of the metal, $\text{Re}(\epsilon_{\text{Au}})$ [54]. The spectral position of the absorption peak is represented by the following resonance condition [44]:

$$\text{Re}(\epsilon_{\text{Au}}) \approx -2\epsilon_{\text{m}}, \quad (7)$$

where ϵ_{m} is the dielectric constant of the surrounding medium, which is equal to n^2 [55–58]. This dependency on the refractive index is clearly evident in the absorption spectra obtained for the spherical, prolate, and oblate nanostructures, as can be seen in Figure 5a–c. The insets in Figure 5a–c depict the variations of the LSPR peak with the refractive index.

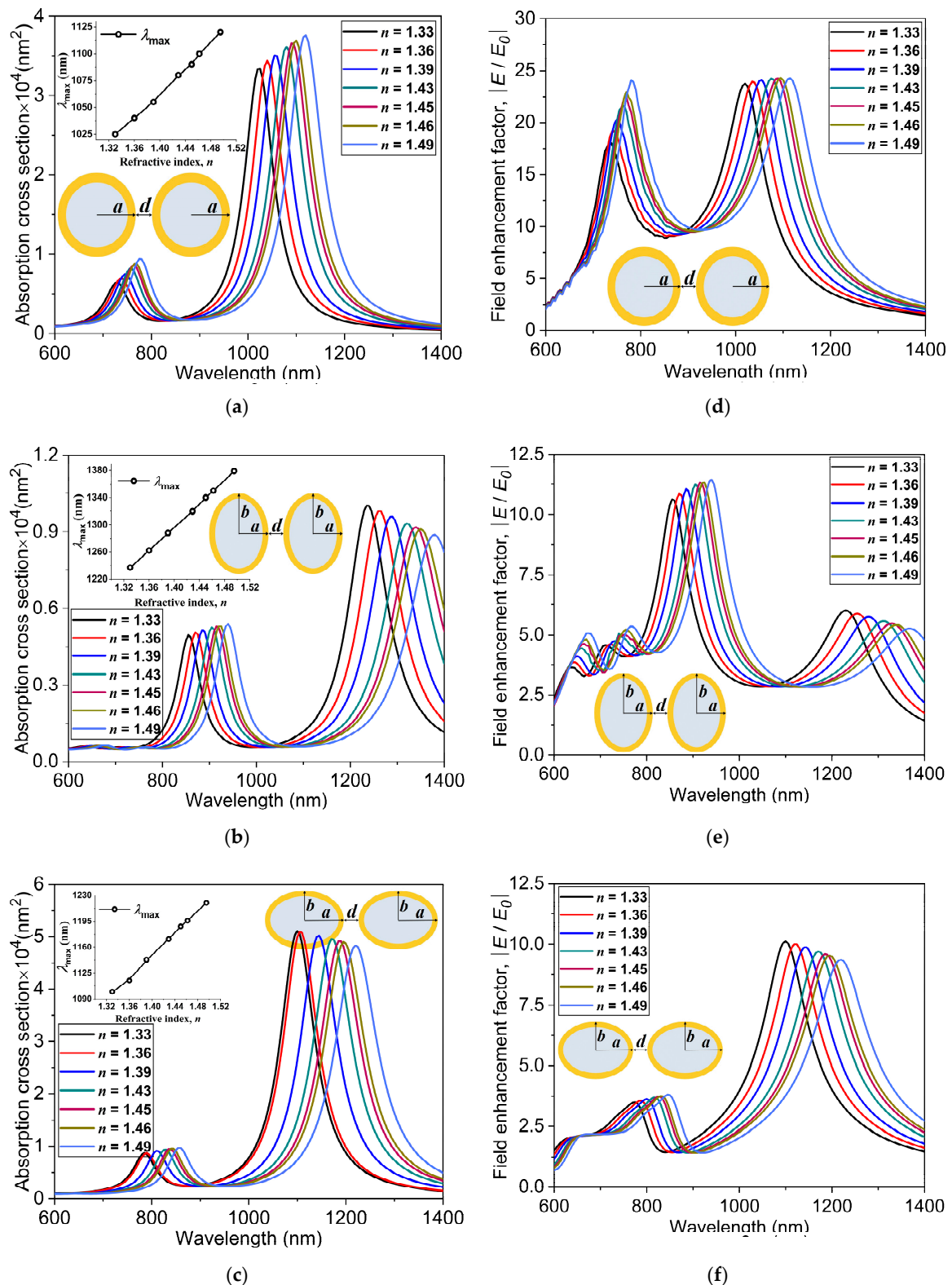


Figure 5. Absorption cross-sections at different refractive indices of the surrounding medium for the (a) spherical ($r = 20 \text{ nm}$, $t_{\text{Au}} = 3 \text{ nm}$), (b) prolate and (c) oblate core-shell nanostructures ($r_{\text{eff}} = 23 \text{ nm}$, $\eta = 3$). The insets in panels (a–c) show the dependence of the LSPR peak positions (λ_{max}) on the refractive index. The electric field enhancement $|E/E_0|$ at different refractive indices for the (d) spherical, (e) prolate, and (f) oblate core-shell nanostructures.

In order to compare our numerical results with experimentally obtained ones, we perform numerical simulations of the hollow AuNS monomer and solid gold nanosphere

monomer with the same dimensions as the experimental study of Sun et al. [59]. Their comparison is presented in Figure 6a. The relative shift in the peak position, $\Delta\lambda_{\max}$, shows linear dependency on the refractive index of the surrounding medium. Here, $\Delta\lambda_{\max}$ is defined as the relative shift in the peak position from the value of gold nanostructure in water, of $n = 1.33$, to indicate its dependency on the refractive index. The nature of the graph shows that the sensitivity factor is a ratio between the relative shift in the peak position, $\Delta\lambda_{\max}$, and the change in the refractive index, Δn (RIU). The sensitivity factors ($\Delta\lambda_{\max}/\Delta n$) given by the slopes in this figure are calculated as 385 nm/RIU and 66 nm/RIU for the AuNS and solid Au nanosphere, respectively. These numerically obtained sensitivity factors are in good agreement with the experimental values, 405 nm/RIU and 62 nm/RIU [59]. In the same manner, the sensitivity factors for the numerically simulated spherical and non-spherical Au nanostructures are computed and shown in Figure 6b. The relative shift in the peak position for the dimer nanostructures clearly shows better sensitivity when compared with the monomer counterparts of solid Au nanosphere and AuNS. The slopes for the three dimer nanostructures indicate that the prolate spheroid dimers are the most sensitive nanostructures among the three types, with a slope of 871.45 nm/RIU. This suggests that a wide range of tunability of LSPR in the NIR-II biological window can be obtained for prolate spheroid dimers with a sensitivity 1.5 times more than the case of the spherical AuNS dimers (577.78 nm/RIU). For different surrounding media considered in this numerical study, the electric field enhancements, $|E/E_0|$, for the spherical, prolate, and oblate Au nanostructure dimers are depicted in Figure 5d–f, respectively. It is noteworthy that as the refractive index increases, the maximum of $|E/E_0|$ in the lower energy mode slightly decreases for the non-spherical nanostructures but remains nearly constant for the spherical AuNS dimer.

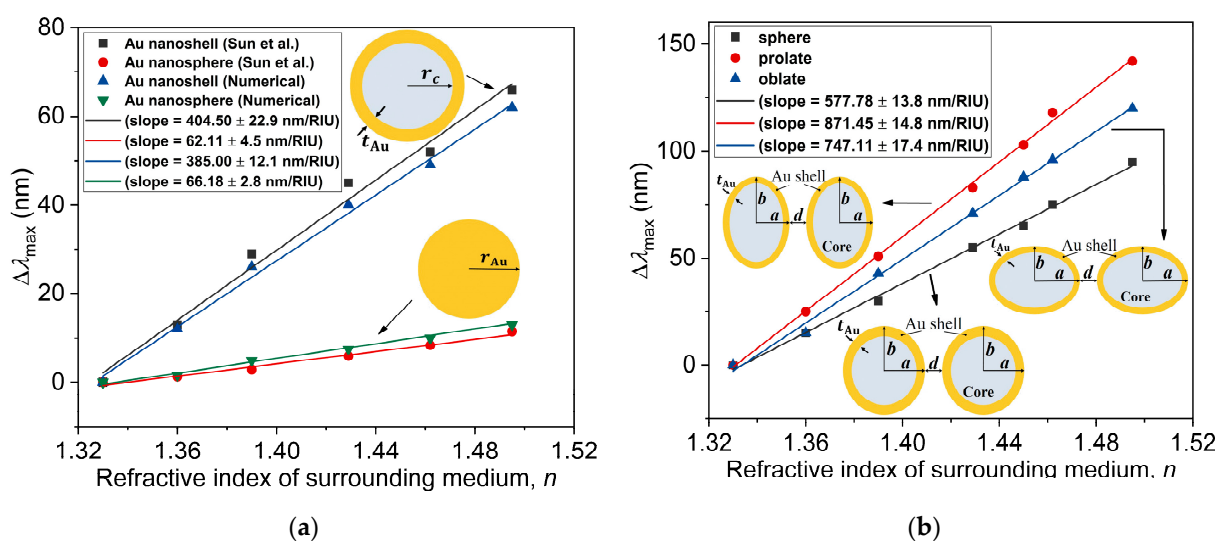


Figure 6. (a) Variations of the relative shift in the peak position (with respect to that for water, $n = 1.33$), $\Delta\lambda_{\max}$, with the refractive index of the surrounding medium for the Au nanoshell ($r_c = 25$ nm, $t_{Au} = 4.5$ nm) and solid Au nanosphere ($r_{Au} = 25$ nm), compared with the experimental study of Sun et al. [59]. (b) Variations of the relative shift in the peak position, $\Delta\lambda_{\max}$, with the refractive index for the spherical ($r = 20$ nm, $t_{Au} = 3$ nm) and non-spherical ($r_{\text{eff}} = 23$ nm, $\eta = 3$) core-shell Au nanostructures. The straight lines in panels (a) and (b) represent the slopes of the data for the nanostructures.

3.5. Au Shell Thickness and Distance of Separation

To further investigate the structure-dependent absorption characteristics of the spherical and non-spherical gold nanostructures, the thickness of the Au shell is considered as a parameter in this subsection. Figure 7 presents the absorption cross-sections at different shell thicknesses for the spherical and non-spherical dimer nanostructures while keeping the effective radius of the nanostructures and distance of separation fixed at $r_{\text{eff}} = 23$ nm

and $d = 1$ nm. In order to see the effect of shell thickness, seven different shell thicknesses, ranging from 1 nm to 5 nm, are selected. The most distinctive feature in the three types of dimer nanostructures is that as the thickness of Au decreases, there is a clear red-shift in the LSPR peaks in the NIR-II window. This obvious red-shift with decreasing thickness can be attributed to an increase in the Au–Au shell interaction, which results in a greater energy separation between higher and lower energy modes [60]. For a shell thickness of 1 nm, the maximum red-shift for the spherical dimer nanostructure is 1591 nm, whereas those for the prolate and oblate nanostructures are 2095 nm and 1794 nm, respectively. The LSPR peaks of the lower energy modes in the longer wavelength region are mainly due to the dipole modes, and the higher energy modes occurring in the shorter wavelength region are due to the plasmon resonant coupling of quadrupole modes. A strong red-shift in the absorption peak for the lower energy resonance occurring in the longer wavelength region corresponds to the plasmon hybridization in the hollow core and outer shell of the dimer nanostructures. This plasmon hybridization in the Au nanostructures gives rise to the antisymmetrically coupled higher energy (antibonding) plasmon mode and a symmetrically coupled lower energy (bonding) plasmon mode [61].

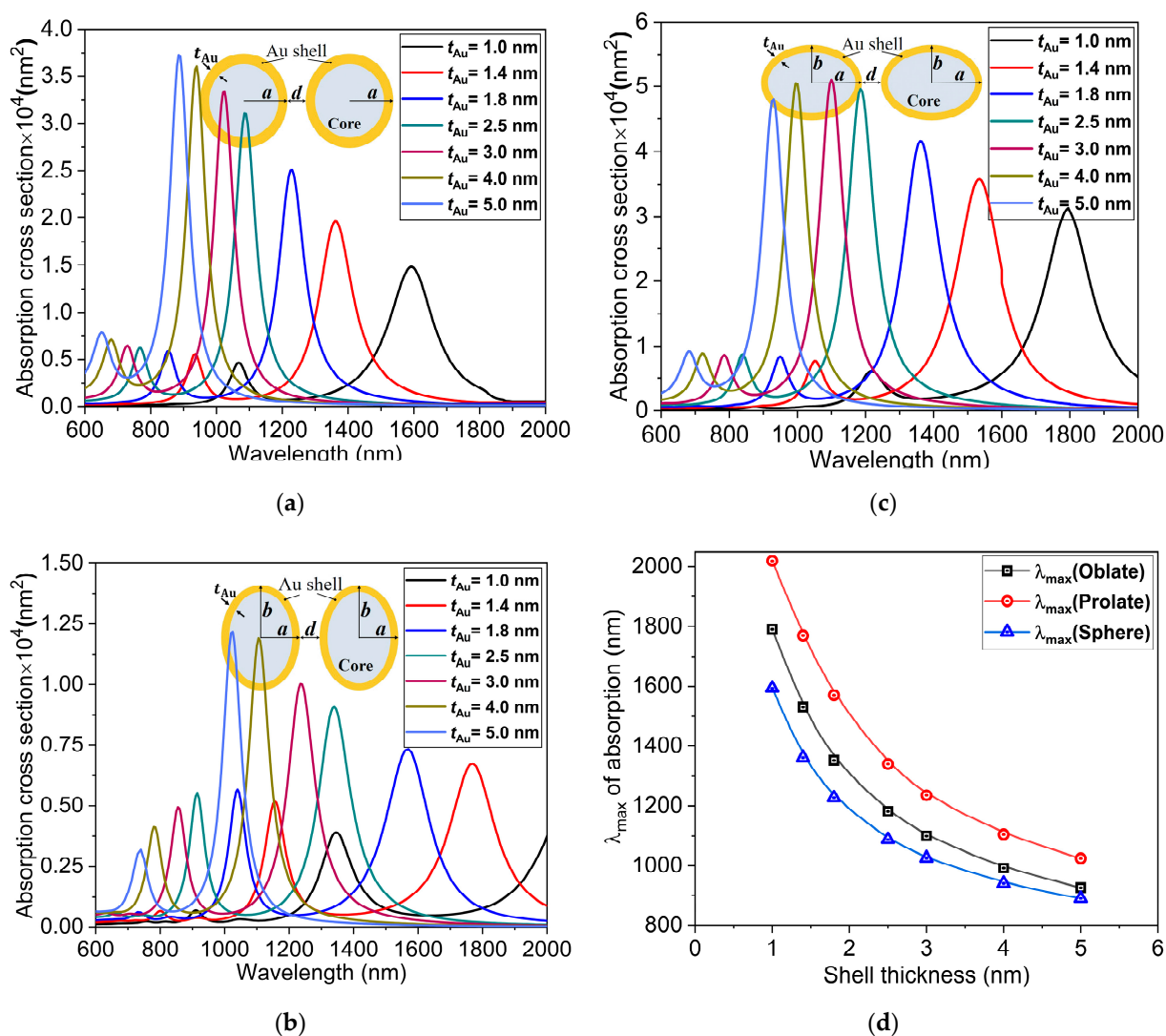


Figure 7. Absorption cross sections at different Au shell thicknesses for the (a) spherical, (b) prolate and (c) oblate Au core-shell nanostructures. (d) Variations of the LSPR peak position (λ_{max}) with the Au shell thickness for the spherical ($r = 20$ nm, $d = 1$ nm) and non-spherical ($r_{\text{eff}} = 23$ nm, $d = 1$ nm) Au core-shell nanostructures.

The evolution of LSPR in the core-shell dimer nanostructures with spherical and non-spherical shapes is numerically investigated and depicted in Figure 8.

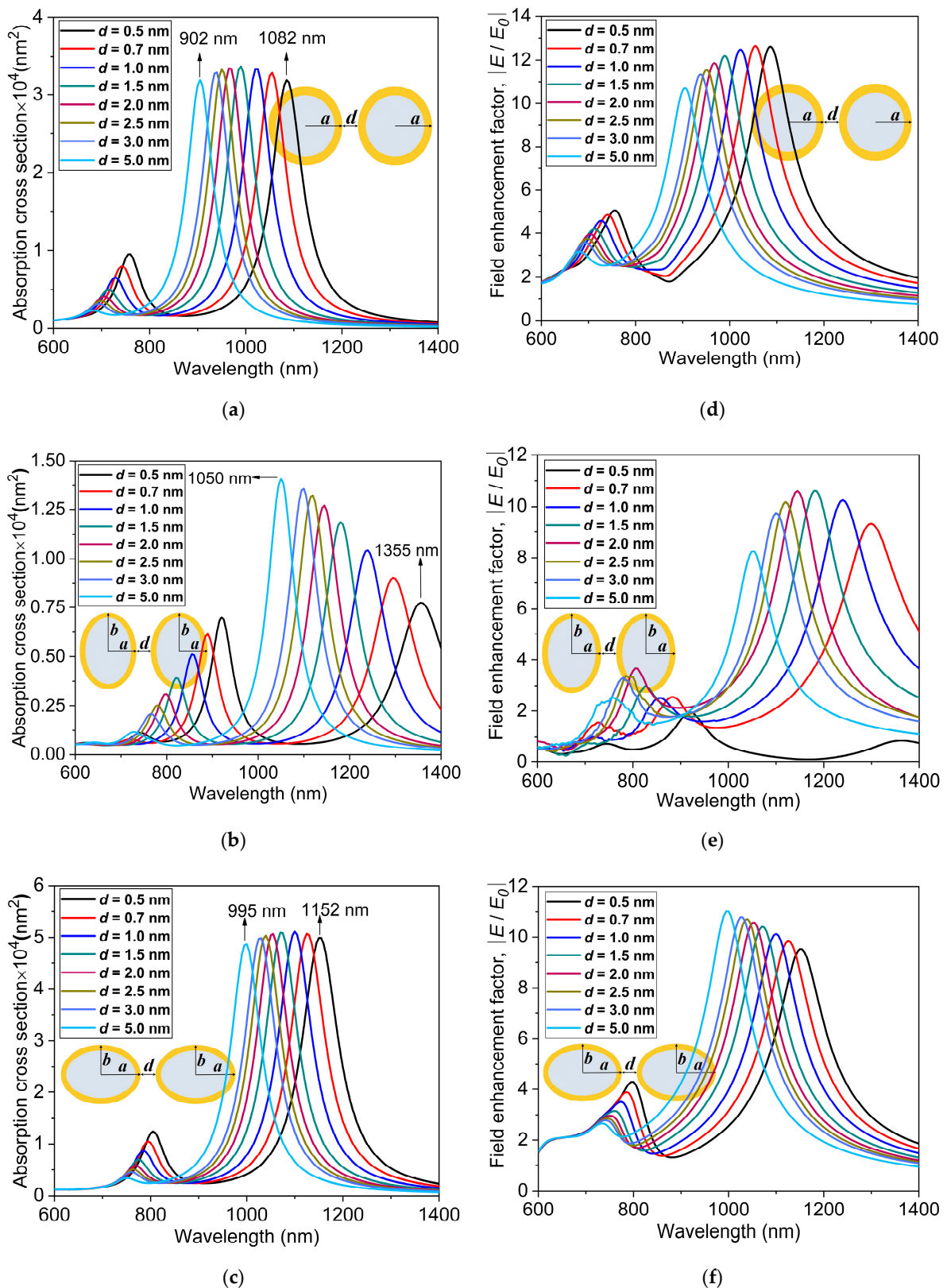


Figure 8. Absorption cross-sections at different distances of separation ($d = 0.5 \text{ nm}$ to 5 nm) for the (a) spherical nanostructure ($r = 20 \text{ nm}$, $t_{\text{Au}} = 3 \text{ nm}$), (b) prolate, and (c) oblate Au core-shell dimer nanostructures ($r_{\text{eff}} = 23 \text{ nm}$, $\eta = 3$). The electric field enhancement factors, $|E/E_0|$, for the (d) spherical, (e) prolate, and (f) oblate nanostructures.

An experimental investigation on the AuNSs using water as the inner core and surrounding material was performed previously [26]. Here, we study the effect of the separation distance (d) between the outer surfaces of spherical ($r = 20$ nm, $t_{\text{Au}} = 3$ nm) and non-spherical ($r_{\text{eff}} = 23$ nm, $\eta = 3$) dimer nanostructures. The total effective radius (r_{eff}) for the prolate and oblate structures is kept the same as the outer radius of the spherical AuNS. Figure 8a–c shows the absorption cross-sections for the spherical, prolate, and oblate Au nanostructures, respectively. As the separation distance between the nanoshells decreases from $d = 5$ nm to 0.5 nm, there is a red-shift in the absorption cross-section peak for the three nanostructures. A significantly stronger interaction of the individual nanostructures due to the dimer configuration with a much smaller distance of separation gives rise to a larger red-shift in the absorption cross-section peak. The most red-shift into the NIR-II window occurs for the least separation distance $d = 0.5$ nm with λ_{max} equal to 1082 nm, 1355 nm, and 1152 nm for the spherical, prolate, and oblate Au nanostructures, respectively. In particular, two distinct resonance peaks are observed in the absorption spectra, one in the longer wavelength region (NIR-II window) and the other in the shorter wavelength region (NIR-I window), as can be seen in Figure 8a–c. The resonance peaks with higher magnitudes in the longer wavelength region occur due to the coupling of the bonding modes in the dimer structure, whereas the peaks with very low magnitudes in the shorter wavelength region are a result of the coupling of the anti-bonding modes of the individual spherical and non-spherical nanostructures [62]. As the distance of separation decreases from $d = 5$ nm to 0.5 nm, the higher energy quadrupole modes in the shorter wavelength region are red-shifted by a small amount, which is in good agreement with previous studies [63,64].

For the same aspect ratio $\eta = 3$, the peaks of absorption cross-sections are above 4×10^4 nm² for the oblate nanostructure, whereas they are well below 2×10^4 nm² for the prolate structures, suggesting that the absorption of the oblate structure is more than twice as large as that of the prolate structure. Interestingly, for the oblate and spherical nanostructures, the peak of absorption is barely influenced by a change in the distance of separation. For the prolate structure, on the other hand, the peak shows greater dependence on the distance of separation and, with increasing distance, drastically increases (1.40×10^4 nm² for $d = 5$ nm to 0.77×10^4 nm² for $d = 0.5$ nm). This dependency and resulting red-shift are due to the strong surface plasmon resonance coupling, indicating a significant electromagnetic interaction between the dimer nanostructures for the distances of separation considered in this study. Figure 8d–f shows the electric field enhancement values, $|E/E_0|$, for the spherical, prolate, and oblate Au dimer nanostructures, respectively. As can be seen in the figures, as the distance of separation increases, the blue-shift in the LSPR peak is observed. For the spherical nanostructure, as the distance of separation increases from 0.5 to 5 nm (see Figure 8f), the electric field enhancement undergoes a slight decrease and the LSPR peak shifts nearly 175 nm towards the shorter wavelength (1085 nm for $d = 0.5$ nm to 910 nm for $d = 5$ nm).

4. Conclusions

In this paper, we presented a numerical analysis of the absorption cross-sections and electromagnetic field enhancement of the spherical and non-spherical core-shell dimer nanostructures by solving the Helmholtz equation, using the complex dielectric function of gold derived from the Drude–Lorentz model. The study is performed by introducing finite element modelling in COMSOL Multiphysics with dimer nanostructures encapsulated by perfectly matched layers (PMLs) and scattering type boundary conditions. The present numerical model is validated by comparing the numerically obtained absorption cross-sections with those of Oldenburg et al. [52]. Upon coupling of two core-shell nanoparticles to form a dimer, the localized surface plasmon resonance (LSPR) peaks are rigorously red-shifted, specifically providing an extensive range of tunability in the NIR-II window. The monomer counterpart with the identical morphology does not exhibit this behaviour since the range of tunability is limited to the NIR-I window. Furthermore, when compared to the

monomer counterparts of gold nanoshell (AuNS), the relative shift in the peak position for dimer nanostructures clearly displays superior sensitivity. In addition, the absorption cross-sections and electric field enhancement at different refractive indices of the surrounding medium, gold shell thicknesses, and distances of separation between the nanostructures are discussed in this paper. The slopes of the relative shift in the peak position for the three dimer nanostructures indicate that the prolate dimers are the most sensitive to change in the refractive index of the surrounding medium, with a wide range of LSPR tunability in the NIR-II biological window. The study shows that the LSPR peak position is influenced more by the thickness of the Au shell than the distance of separation between the nanostructures. The results reported here can be crucial in biomedical applications for accurately predicting the optical properties of gold nanostructures.

Author Contributions: Conceptualization, J.F. and S.K.; methodology, J.F.; software, J.F.; validation, J.F.; formal analysis, J.F.; investigation, J.F.; writing—original draft preparation, J.F.; writing—review and editing, S.K.; supervision, S.K.; project administration, S.K.; funding acquisition, S.K. All authors have read and agreed to the published version of the manuscript.

Funding: This research received no external funding.

Institutional Review Board Statement: Not applicable.

Informed Consent Statement: Not applicable.

Data Availability Statement: The data presented in this study are available on request from the corresponding author.

Acknowledgments: This research has been financially supported by the Basic Science Research Programs through the National Research Foundation of Korea (NRF), funded by the Ministry of Education (2020R1I1A3070105).

Conflicts of Interest: The authors declare no conflict of interest.

References

1. Saha, K.; Agasti, S.S.; Kim, C.; Li, X.; Rotello, V.M. Gold nanoparticles in chemical and biological sensing. *Chem. Rev.* **2012**, *112*, 2739–2779. [[CrossRef](#)] [[PubMed](#)]
2. Pang, B.; Yang, X.; Xia, Y. Putting gold nanocages to work for optical imaging, controlled release and cancer theranostics. *Nanomedicine* **2016**, *11*, 1715–1728. [[CrossRef](#)] [[PubMed](#)]
3. Loo, C.; Lowery, A.; Halas, N.; West, J.; Drezek, R. Immunotargeted nanoshells for integrated cancer imaging and therapy. *Nano Lett.* **2005**, *5*, 709–711. [[CrossRef](#)] [[PubMed](#)]
4. Hirsch, L.R.; Jackson, J.B.; Lee, A.; Halas, N.J.; West, J.L. A whole blood immunoassay using gold nanoshells. *Anal. Chem.* **2003**, *75*, 2377–2381. [[CrossRef](#)]
5. Ren, Y.; Qi, H.; Chen, Q.; Ruan, L. Thermal dosage investigation for optimal temperature distribution in gold nanoparticle enhanced photothermal therapy. *Int. J. Heat Mass Transf.* **2017**, *106*, 212–221. [[CrossRef](#)]
6. Abadeer, N.S.; Murphy, C.J. Recent progress in cancer thermal therapy using gold nanoparticles. *J. Phys. Chem. C* **2016**, *120*, 4691–4716. [[CrossRef](#)]
7. Jain, P.K.; Lee, K.S.; El-Sayed, I.H.; El-Sayed, M.A. Calculated absorption and scattering properties of gold nanoparticles of different size, shape, and composition: Applications in biological imaging and biomedicine. *J. Phys. Chem. B* **2006**, *110*, 7238–7248. [[CrossRef](#)]
8. Del Fatti, N.; Christofilos, D.; Vallée, F. Optical response of a single gold nanoparticle. *Gold Bull.* **2008**, *41*, 147–158. [[CrossRef](#)]
9. Averitt, R.D.; Westcott, S.L.; Halas, N.J. Linear optical properties of gold nanoshells. *J. Opt. Soc. Am. B* **1999**, *16*, 1824. [[CrossRef](#)]
10. McConnell, W.P.; Novak, J.P.; Brousseau, L.C.; Fuierer, R.R.; Tenent, R.C.; Feldheim, D.L. Electronic and optical properties of chemically modified metal nanoparticles and molecularly bridged nanoparticle arrays. *J. Phys. Chem. B* **2000**, *104*, 8925–8930. [[CrossRef](#)]
11. Kreibitz, U.; Vollmer, M. *Optical Properties of Metal Clusters*; Springer Series in Materials Science; Springer: Berlin/Heidelberg, Germany, 1995; Volume 25, ISBN 978-3-642-08191-0.
12. Faraday, M.X. The Bakerian Lecture—Experimental relations of gold (and other metals) to light. *Philos. Trans. R. Soc. Lond.* **1857**, *147*, 145–181. [[CrossRef](#)]
13. Lee, K.S.; El-Sayed, M.A. Dependence of the enhanced optical scattering efficiency relative to that of absorption for gold metal nanorods on aspect ratio, size, end-cap shape, and medium refractive index. *J. Phys. Chem. B* **2005**, *109*, 20331–20338. [[CrossRef](#)]
14. Soni, S.; Tyagi, H.; Taylor, R.A.; Kumar, A. Investigation on nanoparticle distribution for thermal ablation of a tumour subjected to nanoparticle assisted thermal therapy. *J. Therm. Biol.* **2014**, *43*, 70–80. [[CrossRef](#)]

15. Larsson, E.M.; Alegret, J.; Käll, M.; Sutherland, D.S. Sensing characteristics of NIR localized surface plasmon resonances in gold nanorings for application as ultrasensitive biosensors. *Nano Lett.* **2007**, *7*, 1256–1263. [CrossRef]
16. Scaffardi, L.B.; Tocho, J.O. Size dependence of refractive index of gold nanoparticles Related content Size dependence of refractive index of gold nanoparticles. *Inst. Phys. Publ. Nanotechnol. Nanotechnol.* **2006**, *17*, 1309–1315. [CrossRef]
17. Chen, H.; Kou, X.; Yang, Z.; Ni, W.; Wang, J. Shape- and size-dependent refractive index sensitivity of gold nanoparticles. *Langmuir* **2008**, *24*, 5233–5237. [CrossRef]
18. Oldenburg, S.J.; Averitt, R.D.; Westcott, S.L.; Halas, N.J. Nanoengineering of optical resonances. *Chem. Phys. Lett.* **1998**, *288*, 243–247. [CrossRef]
19. Haynes, C.L.; Van Duyne, R.P. Nanosphere lithography: A versatile nanofabrication tool for studies of size-dependent nanoparticle optics. *J. Phys. Chem. B* **2001**, *105*, 5599–5611. [CrossRef]
20. Bao, H.; Yan, C.; Wang, B.; Fang, X.; Zhao, C.Y.; Ruan, X. Double-layer nanoparticle-based coatings for efficient terrestrial radiative cooling. *Solar Energy Mater. Solar Cells* **2017**, *168*, 78–84. [CrossRef]
21. Ren, Y.; Qi, H.; Chen, Q.; Wang, S.; Ruan, L. Localized surface plasmon resonance of nanotriangle dimers at different relative positions. *J. Quant. Spectrosc. Radiat. Transf.* **2017**, *199*, 45–51. [CrossRef]
22. Huang, X.; Qian, W.; El-Sayed, I.H.; El-Sayed, M.A. The potential use of the enhanced nonlinear properties of gold nanospheres in photothermal cancer therapy. *Lasers Surg. Med.* **2007**, *39*, 747–753. [CrossRef] [PubMed]
23. Jain, P.K.; El-Sayed, M.A. Universal scaling of plasmon coupling in metal nanostructures: Extension from particle pairs to nanoshells. *Nano Lett.* **2007**, *7*, 2854–2858. [CrossRef] [PubMed]
24. Liang, H.P.; Wan, L.J.; Bai, C.L.; Jiang, L. Gold hollow nanospheres: Tunable surface plasmon resonance controlled by interior-cavity sizes. *J. Phys. Chem. B* **2005**, *109*, 7795–7800. [CrossRef] [PubMed]
25. Schwartzberg, A.M.; Olson, T.Y.; Talley, C.E.; Zhang, J.Z. Synthesis, characterization, and tunable optical properties of hollow gold nanospheres. *J. Phys. Chem. B* **2006**, *110*, 19935–19944. [CrossRef] [PubMed]
26. Xie, H.N.; Larmour, I.A.; Chen, Y.C.; Wark, A.W.; Tileli, V.; McComb, D.W.; Faulds, K.; Graham, D. Synthesis and NIR optical properties of hollow gold nanospheres with LSPR greater than one micrometer. *Nanoscale* **2012**, *5*, 765–771. [CrossRef] [PubMed]
27. Koike, N.; Ikuno, T.; Okubo, T.; Shimojima, A. Synthesis of monodisperse organosilica nanoparticles with hollow interiors and porous shells using silica nanospheres as templates. *Chem. Commun.* **2013**, *49*, 4998–5000. [CrossRef] [PubMed]
28. Choi, M.R.; Stanton-Maxey, K.J.; Stanley, J.K.; Levin, C.S.; Bardhan, R.; Akin, D.; Badve, S.; Sturgis, J.; Robinson, J.P.; Bashir, R.; et al. A cellular trojan horse for delivery of therapeutic nanoparticles into tumors. *Nano Lett.* **2007**, *7*, 3759–3765. [CrossRef]
29. Gobin, A.M.; Lee, M.H.; Halas, N.J.; James, W.D.; Drezek, R.A.; West, J.L. Near-infrared resonant nanoshells for combined optical imaging and photothermal cancer therapy. *Nano Lett.* **2007**, *7*, 1929–1934. [CrossRef]
30. Hatef, A.; Fortin-Deschênes, S.; Boulais, E.; Lesage, F.; Meunier, M. Photothermal response of hollow gold nanoshell to laser irradiation: Continuous wave, short and ultrashort pulse. *Int. J. Heat Mass Transf.* **2015**, *89*, 866–871. [CrossRef]
31. Bardhan, R.; Lal, S.; Joshi, A.; Halas, N.J. Theranostic nanoshells: From probe design to imaging and treatment of cancer. *Acc. Chem. Res.* **2011**, *44*, 936–946. [CrossRef]
32. Shetty, A.; Elliott, A.M.; Schwartz, J.A.; Wang, J.; Esparza-Coss, E.; Klumpp, S.; Taylor, B.; Hazle, J.D.; Stafford, R.J. Use of Gold Nanoshells to Mediate Heating Induced Perfusion Changes in Prostate Tumors. In Proceedings of the Photonic Therapeutics and Diagnostics IV, SPIE, San Jose, CA, USA, 8 February 2008; Volume 6842, p. 68420S.
33. Hatef, A.; Meunier, M. Plasma-mediated photothermal effects in ultrafast laser irradiation of gold nanoparticle dimers in water. *Opt. Express* **2015**, *23*, 1967. [CrossRef]
34. Jiang, Y.; Upputuri, P.K.; Xie, C.; Lyu, Y.; Zhang, L.; Xiong, Q.; Pramanik, M.; Pu, K. Broadband absorbing semiconducting polymer nanoparticles for photoacoustic imaging in second near-infrared window. *Nano Lett.* **2017**, *17*, 4964–4969. [CrossRef]
35. Sun, T.; Dou, J.H.; Liu, S.; Wang, X.; Zheng, X.; Wang, Y.; Pei, J.; Xie, Z. Second Near-Infrared Conjugated Polymer Nanoparticles for Photoacoustic Imaging and Photothermal Therapy. *ACS Appl. Mater. Interfaces* **2018**, *10*, 7919–7926. [CrossRef]
36. Ding, X.; Liow, C.H.; Zhang, M.; Huang, R.; Li, C.; Shen, H.; Liu, M.; Zou, Y.; Gao, N.; Zhang, Z.; et al. Surface plasmon resonance enhanced light absorption and photothermal therapy in the second near-infrared window. *J. Am. Chem. Soc.* **2014**, *136*, 15684–15693. [CrossRef]
37. Tsai, M.F.; Chang, S.H.G.; Cheng, F.Y.; Shanmugam, V.; Cheng, Y.S.; Su, C.H.; Yeh, C.S. Au nanorod design as light-absorber in the first and second biological near-infrared windows for in vivo photothermal therapy. *ACS Nano* **2013**, *7*, 5330–5342. [CrossRef]
38. Maestro, L.M.; Haro-González, P.; Del Rosal, B.; Ramiro, J.; Caamaño, A.J.; Carrasco, E.; Juarranz, A.; Sanz-Rodríguez, F.; Solé, J.G.; Jaque, D. Heating efficiency of multi-walled carbon nanotubes in the first and second biological windows. *Nanoscale* **2013**, *5*, 7882–7889. [CrossRef]
39. Furlani, E.P.; Karampelas, I.H.; Xie, Q. Analysis of pulsed laser plasmon-assisted photothermal heating and bubble generation at the nanoscale. *Lab Chip* **2012**, *12*, 3707–3719. [CrossRef]
40. Moroz, A. Electron mean-free path in metal-coated nanowires. *J. Opt. Soc. Am. B* **2011**, *28*, 1130. [CrossRef]
41. Blaber, M.G.; Arnold, M.D.; Ford, M.J. Search for the ideal lasmonic nanoshell: The effects of surface scattering and alternatives to gold and silver. *J. Phys. Chem. C* **2009**, *113*, 3041–3045. [CrossRef]
42. Handbook of Optical Constants of Solids—1st Edition. Available online: <https://www.elsevier.com/books/handbook-of-optical-constants-of-solids/palik/978-0-08-055630-7> (accessed on 1 April 2021).

43. Ye, Y.; Chen, T.P.; Liu, Z.; Yuan, X. Effect of Surface Scattering of Electrons on Ratios of Optical Absorption and Scattering to Extinction of Gold Nanoshell. *Nanoscale Res. Lett.* **2018**, *13*, 299. [[CrossRef](#)]
44. Faucheaux, J.A.; Stanton, A.L.D.; Jain, P.K. Plasmon resonances of semiconductor nanocrystals: Physical principles and new opportunities. *J. Phys. Chem. Lett.* **2014**, *5*, 976–985. [[CrossRef](#)]
45. Sikdar, D.; Cheng, W.; Premaratne, M. Optically resonant magneto-electric cubic nanoantennas for ultra-directional light scattering. *J. Appl. Phys.* **2015**, *117*, 083101. [[CrossRef](#)]
46. Flatau, P.J.; Draine, B.T. Fast near field calculations in the discrete dipole approximation for regular rectilinear grids. *Opt. Express* **2012**, *20*, 1247. [[CrossRef](#)]
47. Ding, S.Y.; You, E.M.; Tian, Z.Q.; Moskovits, M. Electromagnetic theories of surface-enhanced Raman spectroscopy. *Chem. Soc. Rev.* **2017**, *46*, 4042–4076. [[CrossRef](#)]
48. Plathier, J.; Merlen, A.; Pignolet, A.; Ruediger, A. Relation between plasmonic tip emission and electromagnetic enhancement evidenced in tip-enhanced Raman spectroscopy. *J. Raman Spectrosc.* **2017**, *48*, 1863–1870. [[CrossRef](#)]
49. Etchegoin, P.G.; Ru, E.C.L. Basic Electromagnetic Theory of SERS. In *Surface Enhanced Raman Spectroscopy: Analytical, Biophysical and Life Science Applications*; Wiley-VCH: Weinheim, Germany, 2010; pp. 1–37. ISBN 9783527325672.
50. Itoh, T.; Yoshida, K.; Biju, V.; Kikkawa, Y.; Ishikawa, M.; Ozaki, Y. Second enhancement in surface-enhanced resonance Raman scattering revealed by an analysis of anti-Stokes and Stokes Raman spectra. *Phys. Rev. B Condens. Matter Mater. Phys.* **2007**, *76*, 085405. [[CrossRef](#)]
51. Xu, H.; Bjerneld, E.J.; Käll, M.; Börjesson, L. Spectroscopy of single hemoglobin molecules by surface enhanced raman scattering. *Phys. Rev. Lett.* **1999**, *83*, 4357–4360. [[CrossRef](#)]
52. Oldenburg, S.J. Light Scattering from Gold Nanoshells. Ph.D. Thesis, Rice University, Houston, TX, USA, 2000.
53. Jeon, H.B.; Tsalu, P.V.; Ha, J.W. Shape Effect on the Refractive Index Sensitivity at Localized Surface Plasmon Resonance Inflection Points of Single Gold Nanocubes with Vertices. *Sci. Rep.* **2019**, *9*, 1–8. [[CrossRef](#)]
54. West, P.R.; Ishii, S.; Naik, G.V.; Emani, N.K.; Shalaev, V.M.; Boltasseva, A. Searching for better plasmonic materials. *Laser Photonics Rev.* **2010**, *4*, 795–808. [[CrossRef](#)]
55. Jahn, M.; Patze, S.; Hidi, I.J.; Knipper, R.; Radu, A.I.; Mühlig, A.; Yüksel, S.; Peksa, V.; Weber, K.; Mayerhöfer, T.; et al. Plasmonic nanostructures for surface enhanced spectroscopic methods. *Analyst* **2016**, *141*, 756–793. [[CrossRef](#)] [[PubMed](#)]
56. Chalmers, J.M.; Griffiths, P.R. *Handbook of Vibrational Spectroscopy, Volume 2*; Chalmers, J.M., Griffiths, P.R., Eds.; J. Wiley: Hoboken, NJ, USA, 2002; ISBN 0471988472.
57. Xia, Y.; Halas, N.J. Shape-controlled synthesis and surface plasmonic properties of metallic nanostructures. *MRS Bull.* **2005**, *30*, 338–343. [[CrossRef](#)]
58. Haes, A.J.; Haynes, C.L.; McFarland, A.D.; Schatz, G.C.; Van Duyne, R.P.; Zou, S. Plasmonic materials for surface-enhanced sensing and spectroscopy. *MRS Bull.* **2005**, *30*, 368–375. [[CrossRef](#)]
59. Sun, Y.; Xia, Y. Increased sensitivity of surface plasmon resonance of gold nanoshells compared to that of gold solid colloids in response to environmental changes. *Anal. Chem.* **2002**, *74*, 5297–5305. [[CrossRef](#)] [[PubMed](#)]
60. Lai, W.; Zhou, J.; Jia, Z.; Petti, L.; Mormile, P. Ag@Au hexagonal nanorings: Synthesis, mechanistic analysis and structure-dependent optical characteristics. *J. Mater. Chem. C* **2015**, *3*, 9726–9733. [[CrossRef](#)]
61. Prodan, E.; Radloff, C.; Halas, N.J.; Nordlander, P. A hybridization model for the plasmon response of complex nanostructures. *Science* **2003**, *302*, 419–422. [[CrossRef](#)]
62. Li, Q.; Zhang, Z. Bonding and anti-bonding modes of plasmon coupling effects in TiO₂-Ag core-shell dimers. *Sci. Rep.* **2016**, *6*. [[CrossRef](#)]
63. Hao, E.; Schatz, G.C. Electromagnetic fields around silver nanoparticles and dimers. *J. Chem. Phys.* **2004**, *120*, 357–366. [[CrossRef](#)]
64. Ruppin, R. Surface modes of two spheres. *Phys. Rev. B* **1982**, *26*, 3440–3444. [[CrossRef](#)]